OPTICAL REVIEW Vol. 20, No. 1 (2013) 19–25

# Visualized Numerical Assessment for Near Infrared Diffuse Optical Tomography with Contrast-and-Size Detail Analysis

Liang-Yu CHEN[1], Min-Cheng PAN[2]*, and Min-Chun PAN[1,3]

[1]*Department of Mechanical Engineering, National Central University, Jhongli, Taoyuan 32001, Taiwan, R.O.C.*
[2]*Department of Electronic Engineering, Tungnan University, New Taipei City 222, Taiwan, R.O.C.*
[3]*Graduate Institute of Biomedical Engineering, National Central University, Jhongli, Taoyuan 32001, Taiwan, R.O.C.*

(Received August 20, 2012; revised October 25, 2012; Accepted November 22, 2012)

The purpose of this study is to propose an objective contrast-and-size detail (CSD) analysis for near infrared diffuse optical tomography (NIR DOT), of which the concept is derived from the subjective contrast detail (CD) analysis. We define a measure for numerical CSD analysis based on the resolution estimation of contrast and size. Following that, the contrast-and-size map of resolution can be calculated and displayed for each corresponding image in the map; furthermore, a CSD resolution curve can be plotted by calculating the average value of the projection corresponding to the physical quantity/axis (size or contrast). To provide some worked examples about the proposed CSD analysis evaluating the imaging performance of different reconstruction methods, Tikhonov regularization and edge-preserving regularization with different weighting functions were employed. Results suggested that using edge-preserving regularization with the generalized Lorentzian weighting function is the most attractive for the estimation of absorption-coefficient images. 

**Keywords:** contrast-and-size detail analysis, diffuse optical tomography, contrast detail analysis, optical-property image

## 1. Introduction

Near infrared (NIR) diffuse optical tomography (DOT) is an emerging technology to imaging through tissue with near-infrared NIR light, which involves both a complex theoretical framework and an advanced experimental instrument. However, a comparison of reconstruction methods is problematic because tools for the objective assessment of image quality have yet to be clearly defined for such a nonlinear reconstruction problem. Moreover, there is a trade-off or inverse correlation between inclusion size and contrast that can be detectable in the reconstruction results, i.e., small size inclusion with higher contrast or large size inclusion with lower contrast can be reconstructed more easily. To determinate minimum detectable contrast level for all size of inclusions, a contrast-detail analysis can be performed to evaluate the imaging performance of different reconstruction methods or systems.

Using contrast-detail (CD) analysis or phantom images, there have been applications to several research fields in mammography, computed tomography (CT), displays for medical applications, and so on. For example, a relationship is experimentally determined through the CD curve in X-ray mammography where the line of minimum detected contrast is plotted for varying sized inclusions located within a tissue simulating breast phantom. A CDMAM 3.4 phantom and custom software designed for automatic computation of the CD curves were to perform a complete evaluation of three clinical digital mammography equipments;[1)] similarly, two digital mammography systems were compared in terms of image quality index and dose efficiency.[2)]

The physical characterization of the five computed radiography systems was assessed by performing a CD analysis with an automatic reading.[3)] A CD analysis was used for three commercially available flat panel detectors, two based on the indirect detection mechanism and one based on the direct detection mechanism.[4)] The study assessed CD performance and effective dose of eight different digital chest radiography systems, in which six observers judged phantom images of each modality and CD curves were constructed from the observer data.[5)]

A method with an extension of standard (receiver-operating characteristic-curve fitting) procedures was proposed to construct CD curves for liver computed tomographic images.[6)] Including liquid crystal displays (LCDs) and cathode-ray tube (CRT) displays for medical applications, five different commercial were compared with their CD performance.[7)] A study was to clarify the relationship between display sizes of high resolution computed tomography images for detecting ground-glass opacity and observer performance using a digital CD phantom.[8)]

CD analysis was used to compare the low-contrast detection capabilities of five expert observers viewing five different contrast targets to obtain CD curves for each scanhead of different array-type scanhead technologies.[9)] A software package (CDRAD analyzer) developed for automated scoring of images was used for the CD evaluation of images.[10)]

In the aspect of DOT, CD analysis was used to evaluate the imaging performance of diffuse optical fluorescence tomography, characterizing spatial resolution limits, signal-to-noise limits, and the trade-off between object contrast and size,[11,12)] of which the threshold (contrast-to-noise ratio, 3) was used to approximate a lowest acceptable noise level in

*E-mail address: m2pan@mail.tnu.edu.tw

the image, as a surrogate measure for human detection of objects[13] as well as to quantify total hemoglobin concentration obtained from multi-modality image-guided near infrared spectroscopy.[14]

As can be seen, CD analysis has become an accepted assessment tool to quantify image quality of several different medical systems. Similarly, in diffuse optical imaging there is a link between inclusion size and minimum contrast for detection, which limits the ability to resolve small inclusions accurately. However, the determination and reproducibility of absolute vanishing detection thresholds for several targets of different contrast by human observers yields a high degree of error; due to the large total observer error, CD analysis may be impractical in a clinical environment, unless there is access to a team of observers specifically and extensively trained in this task; i.e., the subjective nature of human perception and the variations in the decision threshold pose limits to the minimum image quality variations detectable with reliability.

We suggest that a computer-based observer may be more reliable for the objective performance of CD analysis as a method for evaluating NIR DOT. Objective methods of assessment of image quality such as numerical measures have the potential to overcome the above limitations. This analysis provides an objective method for assessing detection and characterization limits and can be applied to future improvements in hardware system architecture as well as reconstruction algorithms. In this study, this analysis approach provides a visualization method based on numerical assessment similar to CD analysis, which is utilized for optical-property images reconstructed with Tikhonov regularization (TR) or edge-preserving regularization (EPR) in this study. Furthermore, a CSD resolution curve can be plotted by calculating the average value of the projection corresponding to the physical quantity/axis (size or contrast). To immune from any uncertainty resulting from experimental work, therefore, no more than numerical simulation is considered in this paper.

## 2. Method

This section describes the image reconstruction algorithms of Tikhonov regularization and edge-preserving regularization with varied regularization weighting functions as well as a method of numerical assessment visualized as CD analysis. In addition, we propose and describe an approach to plotting a CSD resolution curve.

### 2.1 *Image reconstruction algorithms*

Such the physical process of NIR light illuminating through a highly-scattering medium can be approximated by a diffusion equation:

$$\nabla \cdot \kappa(\mathbf{r})\nabla\Phi(\mathbf{r},\omega) - \left[\mu_{\mathrm{a}}(\mathbf{r}) - \frac{i\omega}{c}\right]\Phi(\mathbf{r},\omega) = -S(\mathbf{r},\omega), \quad (1)$$

where $\Phi(\mathbf{r},\omega)$ is the photon fluence rate at position $\mathbf{r}$ and $\omega$ is the light modulation frequency, $S(\mathbf{r},\omega)$ is the isotropic source term and $c$ is the speed of light in tissue, as well as $\mu_{\mathrm{a}}$ and $\kappa$ denote the optical absorption and diffusion coefficients, respectively. For solving Eq. (1), finite-element-method based on the Galerkin weak form of Eq. (1) along with a boundary condition, $-\kappa\nabla\Phi\cdot\hat{n} = \alpha\Phi$ (*flux* in fact), is implemented. Thus the following discrete equations in a matrix form,

$$\underbrace{\begin{bmatrix} \mathbf{A}_{ij}^{bb} - \alpha\mathbf{B}_{ij}^{bb} & \mathbf{A}_{ij}^{bI} \\ \mathbf{A}_{ij}^{Ib} & \mathbf{A}_{ij}^{II} \end{bmatrix}}_{\text{optical-property matrix}} \underbrace{\begin{Bmatrix} \mathbf{\Phi}_j^b \\ \mathbf{\Phi}_j^I \end{Bmatrix}}_{\text{fluence rate matrix}} = \underbrace{\begin{Bmatrix} \mathbf{C}_i^b \\ \mathbf{C}_i^I \end{Bmatrix}}_{\text{source matrix}} \quad (2)$$

can be obtained. More detail in derivation can be found in Ref. 15. Obviously, the forward solution, $\mathbf{\Phi}$, can be evaluated through Eq. (2). In terms of the physical process, the fluence rate matrix is quantitatively and qualitatively dependent upon the source matrix and the optical-property matrix, respectively, where the optical-property matrix is the inertia of the material in spite of relating to the wavelength.

For simplicity, Eq. (2) can be expressed as

$$\mathbf{A\Phi} = \mathbf{C}, \quad (3)$$

where $A$ and $C$ are matrices dependent on the optical properties and the source-detection locations, respectively. The forward solution, $\mathbf{\Phi}$, can be explicitly evaluated by Eq. (3). Partially differentiating Eq. (3) with $\partial/\partial\boldsymbol{\mu}_{\mathrm{a}}$ and $\partial/\partial\boldsymbol{\kappa}$, respectively, yields

$$\mathbf{\Phi}' = -\mathbf{A}^{-1}\mathbf{A}'\mathbf{\Phi} + \mathbf{A}^{-1}\mathbf{C}'. \quad (4)$$

With an approximation to applying the Taylor expansion method and ignoring higher order terms, we obtain

$$\mathbf{J}\Delta\boldsymbol{\chi} = \Delta\mathbf{\Phi}, \quad (5)$$

where the Jacobian matrix $\mathbf{J}$ denotes the matrix consisting of $\partial\mathbf{\Phi}/\partial\boldsymbol{\mu}_{\mathrm{a}}$ and $\partial\mathbf{\Phi}/\partial\boldsymbol{\kappa}$, $\Delta\boldsymbol{\chi}$ is the vector composed of $\Delta\boldsymbol{\mu}_{\mathrm{a}}$ and $\Delta\boldsymbol{\kappa}$, and $\Delta\mathbf{\Phi}$ is the vector with differences between calculated photon fluence rate ($\mathbf{\Phi}^{\mathrm{cal}}$) and measured photon fluence rate ($\mathbf{\Phi}^{\mathrm{meas}}$). Then, the elements of the Jacobian matrix can be calculated from Eq. (4).

It is known that to solve Eq. (5) is an ill-posed problem. Tikhonov regularization is a method stabilizing the inverse problem through incorporating a priori assumptions to constraint the desired solution. Generally, Tikhonov regularization is to optimize this ill-conditioned problem as

$$\min_{\Delta\boldsymbol{\chi}} \|\mathbf{J}\Delta\boldsymbol{\chi} - \Delta\mathbf{\Phi}\|^2 \text{ subject to } \|\Delta\boldsymbol{\chi}\|^2. \quad (6)$$

We seek a solution to the constrained objective function

$$\mathrm{O} = \|\mathbf{J}\Delta\boldsymbol{\chi} - \Delta\mathbf{\Phi}\|^2 + \lambda\|\Delta\boldsymbol{\chi}\|^2 \quad (7)$$

with the condition

$$\min_{\Delta\boldsymbol{\chi}}\{\mathrm{O}\} = \min_{\Delta\boldsymbol{\chi}}\{\|\mathbf{J}\Delta\boldsymbol{\chi} - \Delta\mathbf{\Phi}\|^2 + \lambda\|\Delta\boldsymbol{\chi}\|^2\}, \quad (8)$$

where $\lambda$ is referred to as the regularization parameter. A solution to Eq. (8) is given by

$$2\mathbf{J}^T(\mathbf{J}\Delta\boldsymbol{\chi} - \Delta\mathbf{\Phi}) + 2\lambda\Delta\boldsymbol{\chi} = 0 \quad (9)$$

and equivalently

$$(\mathbf{J}^T\mathbf{J} + \lambda\mathbf{I})\Delta\boldsymbol{\chi} = \mathbf{J}^T\Delta\mathbf{\Phi}, \quad (10)$$

where Eq. (10) is a constrained estimate of $\Delta\boldsymbol{\chi}$ achieved from Tikhonov regularization.

In an edge-preserving regularization algorithm, the objective function is composed of a residual term and a regularization term where a potential function with edge-preserving properties is introduced into the regularized term; it is desirable to be able to incorporate varied weighting functions into the regularization term to achieve a high-quality result of NIR DOT. Along with the help of half-quadratic regularization to simplify the problem of non-linearity shown in the original proposed objective function, the transformed objective function for NIR DOT can then be written[16,17] as

$$Q^*_{\mathrm{Ep}}(\Delta\boldsymbol{\chi},\mathbf{b}) = \|\mathbf{J}\Delta\boldsymbol{\chi} - \Delta\boldsymbol{\Phi}\|_2^2 + \lambda^2 \sum_l \sum_k \{(\mathbf{b}_l)_k (\mathbf{D}_l\Delta\boldsymbol{\chi})_k^2 + \varphi[(\mathbf{b}_l)_k]\}, \quad (11)$$

where the auxiliary variable $\mathbf{b} = (\mathbf{b}_1, \mathbf{b}_2, \ldots, \mathbf{b}_l, \ldots)$ is introduced by half-quadratic regularization and capable of making Eq. (11) linear in $\Delta\boldsymbol{\chi}$ when performing a minimization task, and $\varphi$ originally determines the regularization imposed on every value of the first-order difference $\mathbf{D}_l\Delta\boldsymbol{\chi}$ which is used to detect the discontinuities of the update vector $\Delta\boldsymbol{\chi}$ in specific direction $l$. In subsequent minimization procedure, $\Delta\boldsymbol{\chi}^n$ is fixed at iteration step $n+1$ and $\mathbf{b}^{n+1}$ is computed using the following expression, i.e.,

$$(\mathbf{b}_l^{n+1})_k = \arg\min_{(\mathbf{b}_l)_k} \{Q^*_{\mathrm{Ep}}(\Delta\boldsymbol{\chi}^n, (\mathbf{b}_l)_k)\} = \frac{\varphi'[(\mathbf{D}_l\Delta\boldsymbol{\chi}^n)_k]}{2(\mathbf{D}_l\Delta\boldsymbol{\chi}^n)_k}. \quad (12)$$

Then the new update vector $\Delta\boldsymbol{\chi}^{n+1}$ is obtained from the minimization of $Q^*_{\mathrm{Ep}}(\Delta\boldsymbol{\chi}, \mathbf{b}^{n+1})$ such that

$$\Delta\boldsymbol{\chi}^{n+1} = \arg\min_{\Delta\boldsymbol{\chi}} \{Q^*_{\mathrm{Ep}}(\Delta\boldsymbol{\chi}, \mathbf{b}^{n+1})\} = [\mathbf{J}^T\mathbf{J} + \lambda^2\boldsymbol{\Delta}_{\mathrm{Ep}}^{n+1}]^{-1}\mathbf{J}^T\Delta\boldsymbol{\Phi}, \quad (13)$$

where $\boldsymbol{\Delta}_{\mathrm{Ep}}^{n+1} = \sum_l \mathbf{D}_l^T\mathbf{B}_l^{n+1}\mathbf{D}_l$ and $\mathbf{B}_l^{n+1} = \mathrm{diag}[(\mathbf{b}_l^{n+1})_k]$. The optical parameters are predicted iteratively with using the update equations, i.e., Eqs. (12) and (13), alternately till the stopping criteria are met. To investigate the effect of the edge-preserving weighting function for NIR DOT, we employed varied functions for $\varphi'(t)/2t$ in Eq. (12). In the study, three functions were investigated,[18] i.e., $(\gamma^2)^m/(\gamma^2+t^2)^m$, $e^{-t^2}$, and $(\alpha/2)t^{\alpha-2}$, which are a generalized Lorentzian (GL) function, an exponential (EXP) function, and a generalized total variation (GTV) function with $\alpha = 1$, respectively.

### 2.2 *Numerical assessment and visualization*

To obtain quantitative information of assessing the reconstructed images in these simulations, two measures[19] (contrast resolution and size resolution) are determined over the region of interest. To define the contrast and size resolution in 1D or 2D domain, the concept originates from the precision and density/saturation, respectively, of which the advantage is flexible to easily implement. The contrast resolution $R^{\mathrm{1D,2D}}_{\mathrm{cont}}$ is defined to evaluate the resolution on the contrast of optical property values of the inclusion relative to the background,

$$R^{\mathrm{1D,2D}}_{\mathrm{contrast}} = \frac{(\overline{\max}^{\mathrm{inclusion}}/\overline{\min}^{\mathrm{background}})_{\mathrm{reconstruction}}}{(\overline{\max}^{\mathrm{inclusion}}/\overline{\min}^{\mathrm{background}})_{\mathrm{exact}}} \quad (14)$$

and

$$R^{\mathrm{1D,2D}}_{\mathrm{contrast}} = 2 - R^{\mathrm{1D,2D}}_{\mathrm{contrast}}, \quad \text{if } 1 < R^{\mathrm{1D,2D}}_{\mathrm{contrast}} < 2, \quad (15)$$

where $\overline{\max}$ and $\overline{\min}$ denote the average of maxima and minima over all the selected inclusion or background regions, because of the possibility of some oscillations in these regions. The size resolution is designed to evaluate the resolution on the size over all inclusions as

$$R^{\mathrm{1D,2D}}_{\mathrm{size}} = \left\{\left[1 - \frac{(\mathrm{MSE}^{\mathrm{inclusion}})_{\mathrm{Recon.2.Exact}}}{(\mathrm{MSE}^{\mathrm{inclusion}})_{\mathrm{Exact.2.baseline}}}\right] R^{\mathrm{1D,2D}}_{\mathrm{contrast}}\right\}^{1/2}, \quad (16)$$

where MSE (mean square error) is calculated over the region of interest, the 1D transection profile through the inclusion or the whole 2D image domain, between the exact value of the inclusion and the reconstruction or baseline value and a baseline value is used with the same as the background optical property. It is noted that the size resolution in Eq. (16) includes the contrast resolution in order to prevent from size overestimation.

Following the above two measures, which are the evaluations on contrast and size, respectively, we integrate both two measures into one for numerical contrast-and-size detail (CSD) analysis to evaluate the performance of the reconstruction algorithms by defining

$$R^{\mathrm{1D,2D}}_{\mathrm{contrast\text{-}size\text{-}detail}} = (R^{\mathrm{1D,2D}}_{\mathrm{size}} \cdot R^{\mathrm{1D,2D}}_{\mathrm{contrast}})^{1/2}. \quad (17)$$

Here, we assign this product of the size resolution and the contrast resolution with equally weighting due to that the size and the optical contrast are all the important features to distinguish the inclusion/tumor from the background tissue. With Eq. (17), the contrast-and-size map of resolution can be, therefore, calculated for each corresponding image in the map as well as imaged for visualization. Similar to CD curves but not judged under a subjective condition, in the contrast-and-size map of numerical assessment, the average value of the projection corresponding to the axis (size or contrast), defined as the resolution index, is determined for each size; this is repeated for all sizes and, thus, a contrast-and-size detail (CSD) resolution curve corresponding to the size can be plotted, representing the resolution ability of contrasts for all sizes. Furthermore, it is subtracted from one to correspond to the minimum detectable range of contrasts for all sizes as a CD curve. As well, the same procedure can be made corresponding to the contrast. The schematic diagram of this approach proposed here is illustrated as Fig. 1.

## 3. Results and Discussion

### 3.1 *Contrast-detail analysis*

CD analysis, which has been well accepted in mammography research and quality control, is commonly used to determine the performance of medical imaging systems for assessing the imaging capabilities as well as medical image reconstruction algorithms for evaluating the reconstructing resolution. In assessing each image, the minimum detectable contrast level is determined for each size; this is repeated for

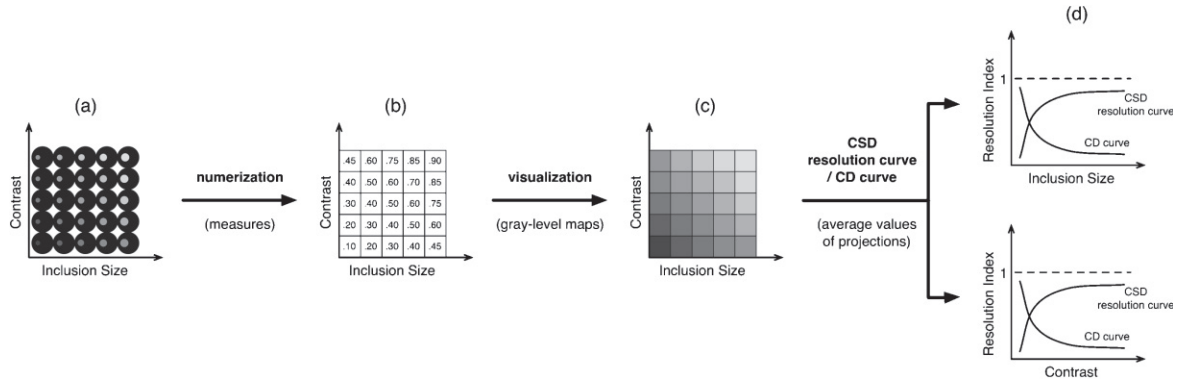


Fig. 1. The schematic diagram of generating a CSD resolution curve. (a) Reconstructing images for a range of inclusion diameters and contrast levels; (b) Calculating contrast-size-detail resolution [Eq. (17)] for each reconstruction images in (a); (c) Generating the contrast-and-size map of resolution by using numerical value in (b) as gray-level intensity; (d) Calculating average contrast-size-detail resolution (resolution index) for each contrast or size, and plotting CSD resolution curve.

all sizes and, thus, a curve can be plotted in the images of contrast-and-size combination, representing the minimum detectable range of contrasts for all sizes.

As described in Sect. 1, only numerical simulation is considered in this study to avoid any interference from experimental phantoms or measurements. For the simulation of this study, it was assumed that 16 measurement locations, equally spaced around the circular circumference, for each of 16 excitation positions were acquired, which yielded a total of 256 amplitude and 256 phase-shift observations for each image reconstruction. Meanwhile, finite-element forward solution with the Robin (type-III) boundary condition was obtained and the finite-element mesh consisting of 4225 nodes and 8192 triangle elements was used to generate simulated data. Although the ideal simulated data had been used to perform the contrast-detail analysis and contrast-and-size detail analysis, the noisy data with randomly generated noise of 1% in amplitude and one degree in phase was employed in the following results. A second mesh consisting of 817 nodes and 1536 triangle elements was generated and used in the image reconstruction procedure to avoid the inverse crime. A breast-like phantom of 80 mm-diameter circular cross section with an inclusion placed along 180° at half-way from center to boundary was used to evaluate the resolving ability of image reconstruction algorithms, of which the homogeneous background has absorption coefficient ($0.01\,\mathrm{mm}^{-1}$) and reduced scattering coefficient ($1\,\mathrm{mm}^{-1}$) as well as the inclusion has 3.5–1.5 : 1 absorption and reduced scattering contrast and a diameter of 5–15 mm. In the meantime, Tikhonov regularization and edge-preserving regularization with different weighting functions in the frequency domain (f = 100 MHz), which were developed into a self-coded software (named as NIR.FD_PC) based on the finite element method, were implemented for the optical-property image reconstruction; to our best of knowledge, image reconstruction using edge-preserving regularization was first applied to NIR DOT in our previous study.[17] All reconstructed images reported in this study started from the optical properties of the homogeneous background, 30

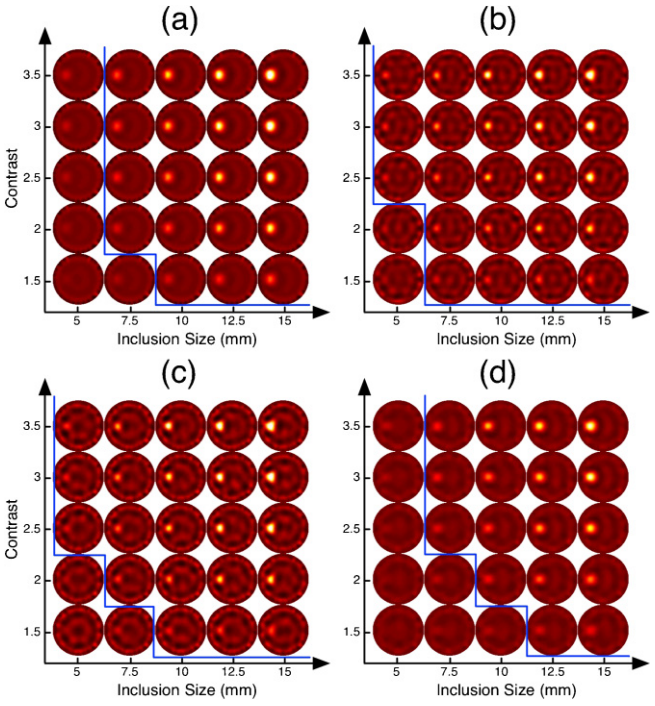


Fig. 2. (Color online) Reconstructions of the absorption images for a range of inclusion diameters and contrast levels. Reconstructed $\mu_a$ images using (a) TR, and (b) EPR with the GL, (c) EXP, (d) GTV weighting function.

iterations were used during the reconstruction procedure and the stopping criterion, $\|\mathbf{\Phi}^{n-1} - \mathbf{\Phi}^{n}\|^2 / \|\mathbf{\Phi}^{n}\|^2 < 10^{-3}$, was met. The cases described as above were reconstructed as shown in Figs. 2 and 3; following this, observer performance study with different contrast-and-size combinations shows CD curves in Figs. 2 and 3 for visual assessments of $\mu_a$ and $\mu_s'$ images reconstructed with four different reconstruction approaches; however, these curves determined were sometimes quite ambiguous.

In the $\mu_a$ images with larger inclusion diameters from 10 to 15 mm, observer performance was better than the images

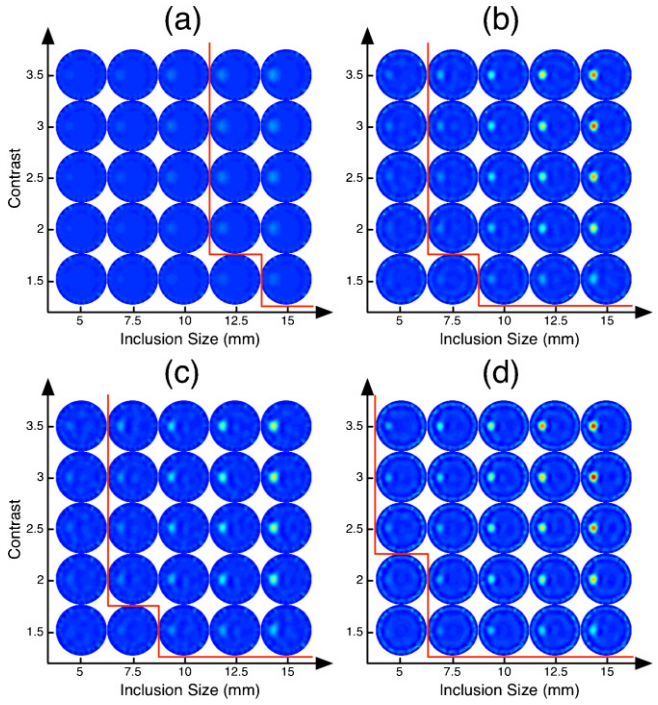


Fig. 3. (Color online) Reconstructions of the reduced scattering images for a range of inclusion diameters and contrast levels. Reconstructed $\mu_s'$ images using (a) TR, and (b) EPR with the GL, (c) EXP, (d) GTV weighting function.

with inclusion diameters of 5 and 7.5 mm but observer performance quite difficultly distinguished from each other of those with a small size inclusion. As a result, analysis on $\mu_s'$ images indicates significant differences but on $\mu_a$ images reveals few differences among different reconstruction approaches; however, we need notice that there is overestimation presenting high contrast for superior visual effects.

### 3.2 *Contrast-and-size detail analysis based on the numerical assessment*

The CD curves showing on the contrast-and-size maps have discussed as above. However, the CD curve is usually determined by expert observers, implying its subjectivity and inconvenience. To overcome the drawbacks of CD analysis, the measure, Eq. (17), was introduced in Sect. 2, which considers the ability to the contrast precision but also the size resolution concerning the performance of an algorithm; much more important to explain, it is emphasized for the measure on its accuracy rather than overestimation.

Therefore, a numerical assessment was achieved with the proposed measure for each image of contrast-and-size combination (Figs. 2 and 3) and it is displayed with its corresponding gray-level value; Fig. 4 shows such those gray-level maps for all images reconstructed from different algorithms. As shown, application of this proposed approach reveals significant differences among these maps; thus, the advantage or weakness of different reconstruction algorithms is judged easily.

In addition, Fig. 5 shows a CSD resolution curve which can be plotted by calculating the average value of the projection corresponding to the physical quantity/axis (size or contrast) in the contrast-and-size map of numerical assessment such as Fig. 4. Definitely, this CSD resolution curve is verified based on numerical calculation, indicating its objectivity and convenience especially either for the comparison among various algorithms or imaging systems. Calculated with the above approach, a set of CSD resolution curves can be established, corresponding to all sizes [Figs. 5(a) and 5(c)] or contrasts [Figs. 5(b) and 5(d)] of Fig. 4 for absorption or reduced scattering images, respectively.

Either from Fig. 4 or 5, we can find that the results show the use of the generalized Lorentzian is superior for the characterization of the absorption coefficients and the generalized total variation for reduced scattering coefficients. For

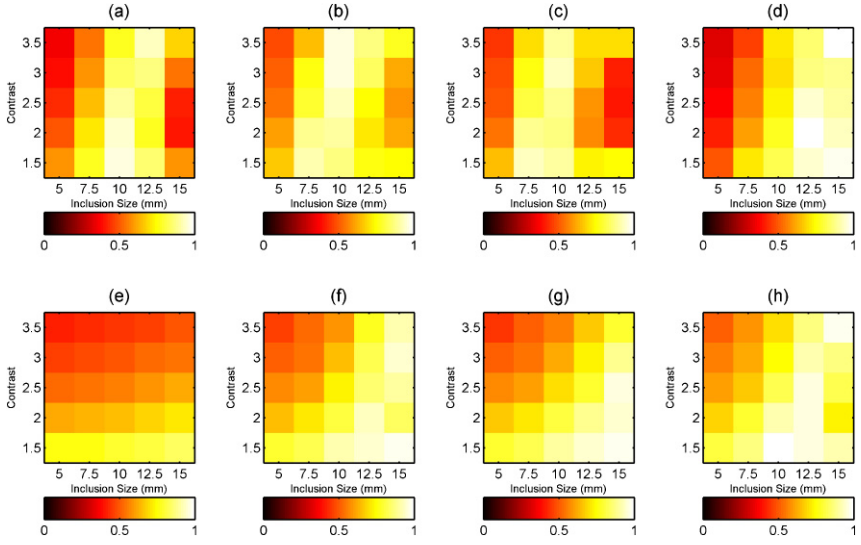


Fig. 4. (Color online) The contrast-and-size map of resolution corresponding to Figs. 2 [(a) to (d)] and 3 [(e) to (h)] by using contrast-size-detail resolution as gray-level intensity.

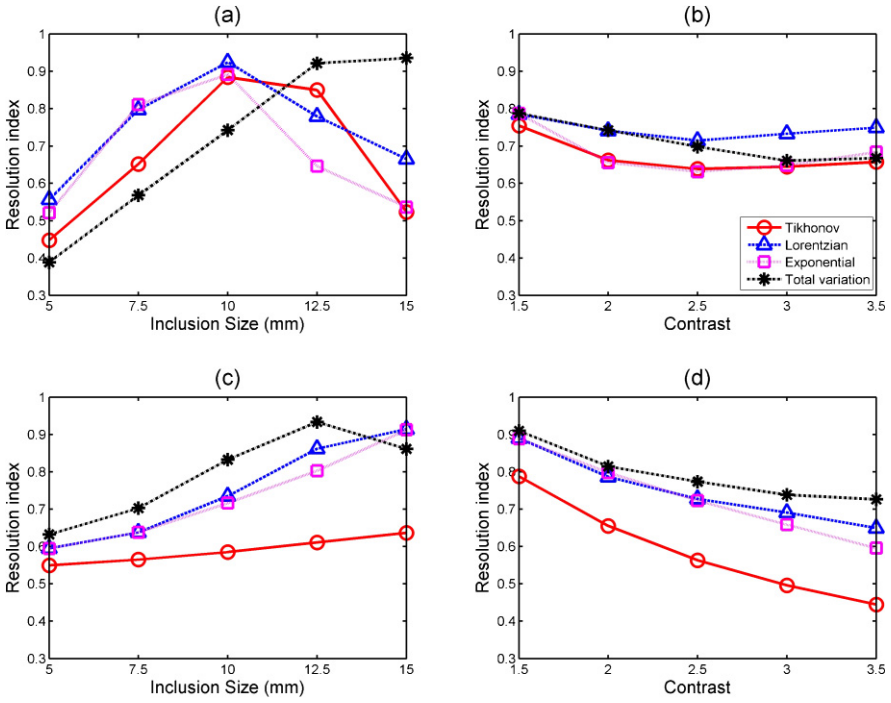


Fig. 5. (Color online) The CSD resolution curve plotted from calculating the average value of the projection corresponding to the axis (size or contrast) in Fig. 4. The CSD resolution curves corresponding to all (a) sizes and (b) contrasts for $\mu_a$ images; the CSD resolution curves corresponding to all (c) sizes and (d) contrasts for $\mu_s'$ images.

the detailed inspection in absorption coefficients [Fig. 5(a)], analysis shows that the generalized Lorentzian performs well and reaches its maximum resolution index of 0.925 for 10-mm-diameter inclusion, whereas the generalized total variation does for larger inclusion of 15-mm-diameter with resolution index 0.936; in spite of this, further analysis in Fig. 5(b) shows that the generalized Lorentzian (with average resolution index 0.745) performs better than the generalized total variation (with average resolution index 0.711) and other reconstruction algorithms. In regard of the reduced scattering coefficients, Fig. 5(c) shows that the generalized total variation works well and has a maximum resolution index of 0.915 for 12.5-mm-diameter inclusion; and Fig. 5(d) also displays that the generalized total variation has better performance for reconstructing the reduced scattering coefficients with maximum resolution index 0.883 at contrast of 1.5. Note that there reveals a interesting trend in Figs. 5(b) and 5(c) where all the maximum resolution indexes of different reconstruction algorithms are present in the lowest contrast. It may indicate that NIR DOT is capable of detecting tumor at low contrast because the optical contrast is the indicator of existence of tumor. In the CD curves of almost all cases from the previous others' work, the ultimate detection limits of 10-mm-diameter inclusions or larger are estimated to show consistent and no differences usually appear among large-size inclusions.

To summarize the current findings, it is suggested that using the edge-preserving regularization associated with the generalized Lorentzian function as a weighting function is the most attractive compared with other functions for the estimation of absorption-coefficient images from which functional information like oxyhemoglobin and deoxyhemoglboin concentration can be characterized.

As have been seen in Figs. 2–5, varied image reconstruction algorithms make obvious difference using CSD analysis rather than using CD analysis; Usually, there is an inverse correlation between inclusion size and contrast as shown in CD curves, which show a superior quality of the evaluated object as the curve approaches to the origin of a CD curve map whereas CSD resolution curves are in a good quality as approaching to a unity.

As well, CSD analysis will be a useful tool when the imaging systems are ongoing in the design stage and being evaluated in various types of architectures to justify use of an optimal design to construct.

## 4. Conclusions

We have developed an approach to assessing reconstruction algorithms, which plots CSD resolution curves enabling an objective evaluation possible. In addition, this approach can provide much more details in which the differences can be differentiated especially among the phantoms with large size inclusions when compared with other methods such as CD analysis. In this study, varied reconstruction algorithms assessed with the proposed approach have been characterized. Furthermore, the proposed approach can plot either CSD resolution curves or CD curves corresponding to the size or contrast as required and be applicable to assess a variety of imaging modalities or algorithms in objectivity.

## References


1) S. Rivetti, N. Lanconelli, R. Campanini, M. Bertolini, G. Borasi, A. Nitrosi, C. Danielli, L. Angelini, and S. Maggi: Med. Phys. **33** (2006) 4198.
2) B. Cederström and U. Streubühr: Nucl. Instrum. Methods Phys. Res., Sect. A **580** (2007) 1101.
3) S. Rivetti, N. Lanconelli, M. Bertolini, A. Nitrosi, A. Burani, and D. Acchiappati: Med. Phys. **37** (2010) 440.
4) G. Borasi, E. Samei, M. Bertolini, A. Nitrosi, and D. Tassoni: Med. Phys. **33** (2006) 1707.
5) W. J. H. Veldkamp, L. J. M. Kroft, M. V. Boot, B. J. A. Mertens, and J. Geleijns: Eur. Radiol. **16** (2006) 333.
6) P. F. Judy, R. G. Swensson, R. D. Nawfel, K. H. Chan, and S. E. Seltzer: Med. Phys. **19** (1992) 1167.
7) E. Samei, N. T. Ranger, and D. M. Delong: Med. Phys. **35** (2008) 1358.
8) M. Yamaguchi, H. Fujita, Y. Bessho, T. Inoue, Y. Asai, and K. Murase: Eur. J. Radiol. **80** (2011) 845.
9) T. J. Hall, M. F. Insana, N. M. Soller, and L. A. Harrison: Med. Phys. **20** (1993) 117.
10) A. Pascoal, C. P. Lawinski, I. Honey, and P. Blake: Phys. Med. Biol. **50** (2005) 5743.
11) B. W. Pogue, S. C. Davis, X. Song, B. A. Brooksby, H. Dehghani, and K. D. Paulsen: J. Biomed. Opt. **11** (2006) 033001.
12) B. W. Pogue, C. Willscher, T. O. McBride, U. L. Osterberg, and K. D. Paulsen: Med. Phys. **27** (2000) 2693.
13) S. C. Davis, B. W. Pogue, H. Dehghani, and K. D. Paulsen: J. Biomed. Opt. **10** (2005) 050501.
14) H. R. Ghadyani, S. Srinivasan, B. W. Pogue, and K. D. Paulsen: Opt. Express **18** (2010) 15917.
15) S. R. Arridge and J. C. Schotland: Inverse Probl. **25** (2009) 123010.
16) P. Charbonnier, L. Blanc-Feraud, G. Aubert, and M. Barlaud: IEEE Trans. Image Process. **6** (1997) 298.
17) L. Y. Chen, M.-C. Pan, and M.-C. Pan: Appl. Opt. **51** (2012) 43.
18) V. B. Surya Prasath and A. Singh: Appl. Math. Comput. **215** (2010) 3655.
19) M.-C. Pan, C. H. Chen, L. Y. Chen, M.-C. Pan, and Y. M. Shyr: J. Biomed. Opt. **13** (2008) 024022.